

Article

# High Selectivity and Stability of Nickel Catalysts for CO<sub>2</sub> Methanation: Support Effects

Jeremías Martínez <sup>1,2,3,\*</sup> , Edgar Hernández <sup>1</sup>, Salvador Alfaro <sup>1</sup> , Ricardo López Medina <sup>4</sup> ,  
Guadalupe Valverde Aguilar <sup>5</sup>, Elim Albiter <sup>1</sup> and Miguel A. Valenzuela <sup>1,\*</sup> 

<sup>1</sup> Lab. Catálisis y Materiales, ESIQIE-Instituto Politécnico Nacional, Zacatenco, Mexico City 07738, Mexico; csicaev@sicaev.com (E.H.); salfahdez@yahoo.com (S.A.); ealbiter@gmail.com (E.A.)

<sup>2</sup> Facultad de Química, Universidad Autónoma del Estado de México, Paseo Colón y Paseo Tollocan S/N, Toluca 50120, Estado de México, Mexico

<sup>3</sup> Centro Conjunto de Investigación en Química Sustentable UAEM-UNAM, Carretera Toluca-Atlacomulco, km 14.5, Toluca 50200, Estado de México, Mexico

<sup>4</sup> Departamento de Energía, Área de Procesos de la Industria Química, Universidad Autónoma Metropolitana, Unidad Azcapotzalco, Mexico City 02200, Mexico; rlopez.ricardo@gmail.com

<sup>5</sup> Centro de Investigación en Ciencia Aplicada y Tecnología Avanzada Unidad Legaria, Instituto Politécnico Nacional, Mexico City 11500, Mexico; valverdeag@gmail.com

\* Correspondence: jmartinezs@uaemex.mx (J.M.); mavalenz@ipn.mx (M.A.V.)

Received: 10 November 2018; Accepted: 24 December 2018; Published: 30 December 2018

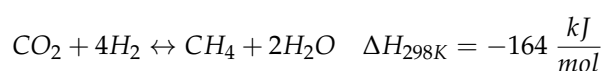


**Abstract:** In this work, we present an investigation concerning the evaluation of the catalytic properties of Ni nanoparticles supported on ZrO<sub>2</sub>, SiO<sub>2</sub>, and MgAl<sub>2</sub>O<sub>4</sub> for CO<sub>2</sub> hydrogenation to methane. The supports were prepared by coprecipitation and sol-gel, while Ni was incorporated by impregnation (10–20 wt %). X-ray diffraction, nitrogen physisorption, temperature-programmed reduction, H<sub>2</sub> pulse chemisorption, Raman spectroscopy, X-ray photoelectron spectroscopy, and transmission electron microscopy were the main characterization techniques employed. A laboratory fixed-bed reactor operated at atmospheric pressure, a temperature range of 350–500 °C, and a stoichiometric H<sub>2</sub>/CO<sub>2</sub> molar ratio was used for catalyst evaluation. The most outstanding results were obtained with nickel catalysts supported on ZrO<sub>2</sub> with CO<sub>2</sub> conversions of close to 60%, and selectivity to methane formation was 100% on a dry basis, with high stability after 250 h of reaction time. The majority presence of tetragonal zirconia, as well as the strong Ni–ZrO<sub>2</sub> interaction, were responsible for the high catalytic performance of the Ni/ZrO<sub>2</sub> catalysts.

**Keywords:** CO<sub>2</sub> methanation; Ni catalysts; ZrO<sub>2</sub>; monoclinic; tetragonal

## 1. Introduction

Carbon dioxide is considered as the greenhouse gas that contributes the most to global warming. Currently, CO<sub>2</sub> concentration in the atmosphere exceeds 400 ppm, a threshold that is extensively accepted as a critical level that could drastically aggravate human-caused global warming [1]. An alternative to the capture and sequestration of CO<sub>2</sub> is its conversion to higher value-added products, such as hydrocarbons, by reacting CO<sub>2</sub> in the presence of hydrogen and heterogeneous catalysts. CO<sub>2</sub> selective hydrogenation (i.e., methanation or Sabatier reaction) is considered as a viable alternative for environmental and energy-related issues, reacting CO<sub>2</sub> with hydrogen to produce methane [2–8]:



This reaction has had growing interest in the last decade, in order to chain the excess of renewable electricity to produce hydrogen, via water electrolysis, with captured and purified CO<sub>2</sub> from waste, to obtain synthetic natural gas (SNG), a concept that is currently referred to as power-to-gas (Ptg) [9].

From the thermodynamic point of view, CO<sub>2</sub> methanation is favored at low temperatures (250–500 °C), high pressures, and H<sub>2</sub>/CO<sub>2</sub> ratios of higher than 4 [9]. Different active metals and supports have been explored for this reaction, and a proof of this are the numerous review articles that have been published in recent years [2–8]. Nickel is the most commonly studied active phase for the CO<sub>2</sub> hydrogenation reaction, supported on materials such as SiO<sub>2</sub>, Al<sub>2</sub>O<sub>3</sub>, TiO<sub>2</sub>, CeO<sub>2</sub> and ZrO<sub>2</sub>, as well as on different combinations of mixed oxides [10–28]. In addition to nickel, a significant number of works using Fe, Ce, Ru, Mn, Pd, Rh, Pt, and Co, as active phases in bimetallic and multi-metallic catalysts have also been used [5,10]. However, noble metals, although they lead to a high selectivity to methane, cannot be compared with Ni, due to their high cost for practical application.

Table S1 summarizes some of the works that have been reported in the open literature for carbon dioxide hydrogenation at atmospheric pressure on nickel catalysts. CO<sub>2</sub> conversions of higher than 90% and selectivity approaching 100% have been found for different nickel catalysts at temperatures ranging from 350 to 400 °C [11,13,14]. The high rates of conversions achieved are directly related to the very low GHSV (<10,000 h<sup>-1</sup>) used in the catalytic test, which result in a longer residence time for the reactant species. A methane selectivity of close to 99%, and a carbon dioxide conversion of about 80%, approaching equilibrium conversion (86%) [15], have been reported for nickel catalysts supported on mixed oxides of cerium and zirconia at atmospheric pressure and 350 °C, at relatively high GHSV (43,000 h<sup>-1</sup>) [2,5,9].

Particularly, ZrO<sub>2</sub> is an effective support for Ni catalysts, inhibiting metal sintering at high temperatures, besides showing high thermal stability and resistance to deactivation by coke formation [29]. On the other hand, ZrO<sub>2</sub> is present mainly in three polymorphs: monoclinic (m-ZrO<sub>2</sub>), tetragonal (t-ZrO<sub>2</sub>), and cubic structures, generating controversy about the role that is played by each type of structure on activity and selectivity [30]. Specifically, in the case of CO<sub>2</sub> methanation, a higher photocatalytic activity is achieved by the use of t-ZrO<sub>2</sub>, which has been explained in terms of a large amount of CO<sub>2</sub> adsorption sites [31].

Regarding the reaction mechanism of CO<sub>2</sub> methanation on Ni/ZrO<sub>2</sub> catalysts, this initiates with the chemisorption of CO<sub>2</sub>, and is followed by its interaction with surface hydroxyl groups on ZrO<sub>2</sub> to give a bicarbonate species that can be reversibly converted to carbonate species. Furthermore, H<sub>2</sub> dissociates on the surface of Ni particles, and it migrates to a reducible metal oxide support by a spillover process, resulting in the formation of surface hydroxyl groups, metal–H species, and formate species. After that, formate species are hydrogenated towards CH<sub>4</sub> formation [32]. In other words, on ZrO<sub>2</sub>-supported nickel catalysts, CO<sub>2</sub> hydrogenation is catalyzed through methane formation by the formate route, rather than by the CO route [7,33].

In this work, nickel catalysts over commercial SiO<sub>2</sub> and synthesized ZrO<sub>2</sub>, and MgAl<sub>2</sub>O<sub>4</sub> supports were evaluated using the same amount of Ni and the same operating conditions. It was found that ZrO<sub>2</sub> showed higher catalytic activity and stability, and the effect of metal loading, the influence of the support synthesis method, and the long-term stability were mainly investigated.

## 2. Results and Discussion

X-ray diffraction (XRD) patterns of the 20 wt % nickel content catalysts supported on SiO<sub>2</sub>, MgAl<sub>2</sub>O<sub>4</sub>, and ZrO<sub>2</sub>-COP are shown in Figure 1. The XRD pattern of the co-precipitated ZrO<sub>2</sub> support consisted of mixed phases. The characteristic peaks of the monoclinic and tetragonal phases are exhibited at 2θ = 24.05, 28.18, and 31.5°, and at 2θ = 29.8, 50.1, and 59.4°, respectively [34,35]. The magnesium aluminate spinel peaks were identified at 2θ values of 19.0, 31.3, 44.9, 59.5, and 63.4° [36], while silicon dioxide is noted at 2θ = 20.9° [37]. The presence of the deposited nickel on the three different supports is evidenced by the characteristic diffraction peaks of nickel oxide at 2θ = 37.3, 43.3, 62.9, 75.4, and 79.4° [38].

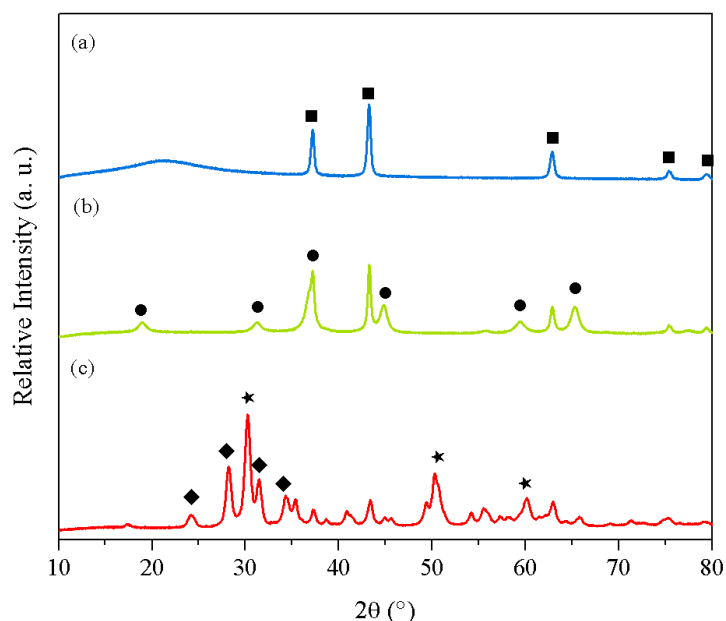


**Figure 1.** X-ray diffraction (XRD) patterns of 20 wt % nickel catalysts. (a) Ni/SiO<sub>2</sub>, (b) Ni/MgAl<sub>2</sub>O<sub>4</sub>, and (c) Ni-ZrO<sub>2</sub>-COP. ZrO<sub>2</sub> Monoclinic phase: (◆), ZrO<sub>2</sub> Tetragonal phase: (★), MgAl<sub>2</sub>O<sub>4</sub> Spinel: (●), NiO: (■).

The results of the catalytic test are presented in Figure 2. An increase in carbon dioxide conversion was observed, with an increase of reaction temperature for all the nickel-based catalysts. A decrease in CO<sub>2</sub> conversion was noticed for 20 wt % Ni/ZrO<sub>2</sub>-COP catalysts at 500 °C, which can be attributed to the sintering of metallic nickel particles [39]. MgAl<sub>2</sub>O<sub>4</sub>-based catalysts with 5 and 10 wt % nickel contents resulted into a higher CO<sub>2</sub> conversion regarding the SiO<sub>2</sub>-based catalyst (Figure 2a,b). The opposite trend was noted when nickel content was increased to 15 and 20 wt % (Figure 2c,d). It was observed that about 50% of CO<sub>2</sub> conversion was achieved with Ni/ZrO<sub>2</sub> catalysts at 400 °C (Figure 2d). Since only carbon dioxide and water were detected in the product analysis, it can be said that the selectivity to methane formation is 100% on a dry basis.

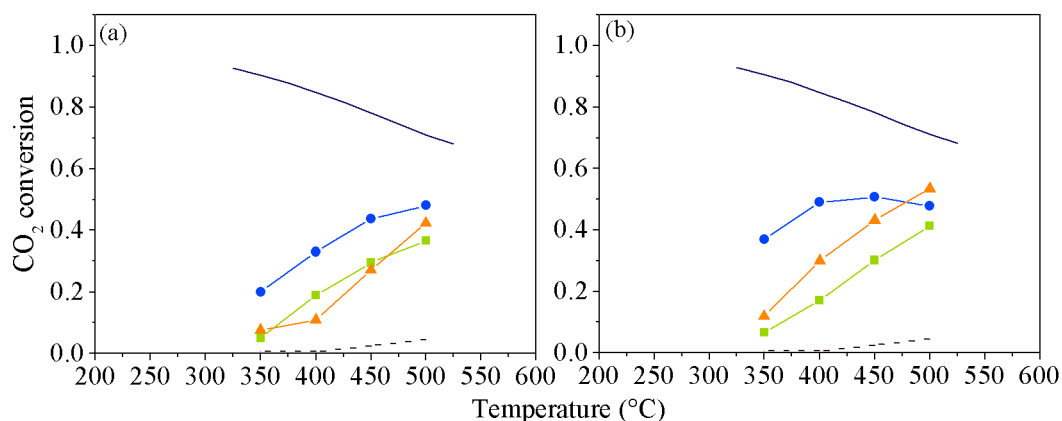


**Figure 2.** Carbon dioxide conversion on nickel-supported catalysts. (a) 10 wt %, (b) 20 wt %. (●) ZrO<sub>2</sub>-COP, (▲) SiO<sub>2</sub>, (■) MgAl<sub>2</sub>O<sub>4</sub>, (dashed line) SiC, (solid line) equilibrium conversion.

Based on these results, the 20 wt % Ni/ZrO<sub>2</sub>-COP catalyst was used for a comparative study of the effect of the support synthesis route on carbon dioxide hydrogenation. The XRD diffraction patterns of synthesized zirconia supports are given in Figure 3. The characteristic diffraction peaks of monoclinic and tetragonal phases were observed in both the co-precipitated and the sol-gel zirconia supports. The Rietveld method was used for the microstructural analysis of the zirconia supports, by processing

X-ray diffraction data by using MAUD software. Microstructural effects such as crystallite size and microdeformations were analyzed by assuming isotropic widening. The calculated patterns produced by the Rietveld model are in good agreement with the experimental X-ray diffraction data. The results of the quantitative phase analysis, refined structural parameters, and crystallite size are given in Table 1. A Rietveld simulation can be seen in Figures S1 and S2. It can be observed that monoclinic zirconia is the predominating phase in the sol-gel support 64%, while in the co-precipitated zirconia, the content of both the monoclinic and tetragonal phases approach to 50%.

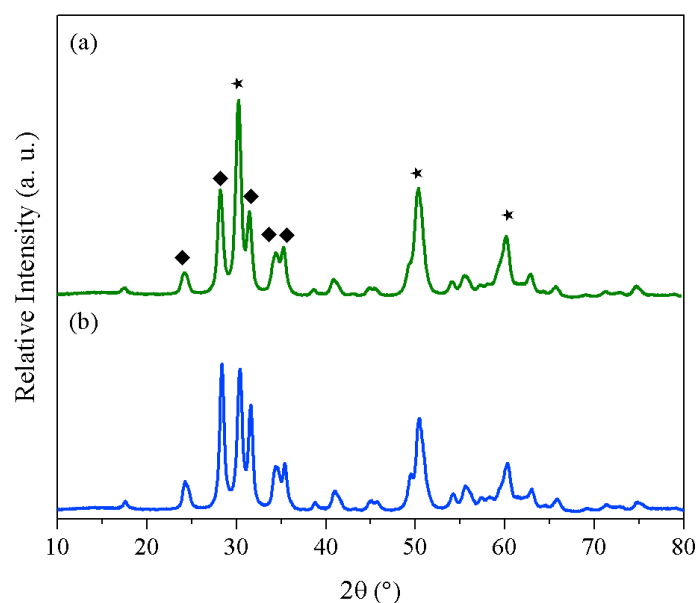


**Figure 3.** XRD diffraction patterns of synthesized zirconia supports. (a) Sol-gel route, (b) Co-precipitation route. ZrO<sub>2</sub> Monoclinic phase: (◆), ZrO<sub>2</sub> Tetragonal phase: (★).

**Table 1.** Phase composition of zirconia supports.

Support	Co-precipitation		Sol-Gel		
	ZrO <sub>2</sub> Phase	Monoclinic	Tetragonal	Monoclinic	Tetragonal
Phase composition, %		47	53	64	36
<sup>a</sup> RSP:		-	-	-	-
A		5.14	3.6	5.15	3.59
B		5.2	3.6	5.2	3.59
C		5.32	5.18	5.32	5.19
Crystallite size, nm		22	18	25	19
Microdeformations		$3.4 \times 10^{-3}$	$2.4 \times 10^{-3}$	$3.0 \times 10^{-3}$	$1.3 \times 10^{-3}$
<sup>b</sup> Rwp (%)			3.56		3.52
<sup>c</sup> Rexp (%)			2.24		2.28

<sup>a</sup> Refined structural parameters; <sup>b</sup> Weighted profile factor; <sup>c</sup> Expected weighted profile factor.

According to the BET analysis, it is observed that the surface area of zirconia is considerably influenced by the preparation method. The specific surface area of zirconia supports, and 20% nickel content zirconia-based catalysts are listed in Table 2. The co-precipitation support resulted in the highest specific surface area (75 m<sup>2</sup>/g), while that of sol-gel zirconia was very low (22 m<sup>2</sup>/g).

Temperature-programmed reduction (TPR) measurements were carried out to analyze the reducibility of supported nickel catalysts, as well as the metal–support interaction. As shown in Figure 4, reduction profiles of the Ni catalysts supported on coprecipitated and sol-gel ZrO<sub>2</sub> were very similar. In both, thermograms could be seen as overlapped peaks, which is characteristic of a strong metal–support interaction effect (SMSI) [40].

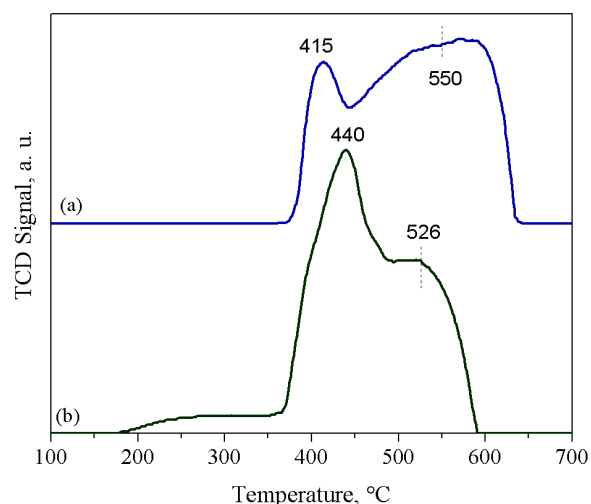


**Figure 4.** Temperature-programmed reduction (TPR) analysis of the 20% Ni catalysts supported on (a) coprecipitated and (b) sol-gel Ni/ZrO<sub>2</sub> catalysts.

**Table 2.** Nitrogen physisorption analysis. Specific surface area and average pore diameter.

Support	Preparation Method	Specific Surface Area (BET), m <sup>2</sup> /g		Average Pore Diameter, nm
		ZrO <sub>2</sub>	20% Ni/ZrO <sub>2</sub>	
ZrO <sub>2</sub> -COP	Co-precipitation	75	53	8.0
ZrO <sub>2</sub> -SG	Sol-Gel	22	19	19.3

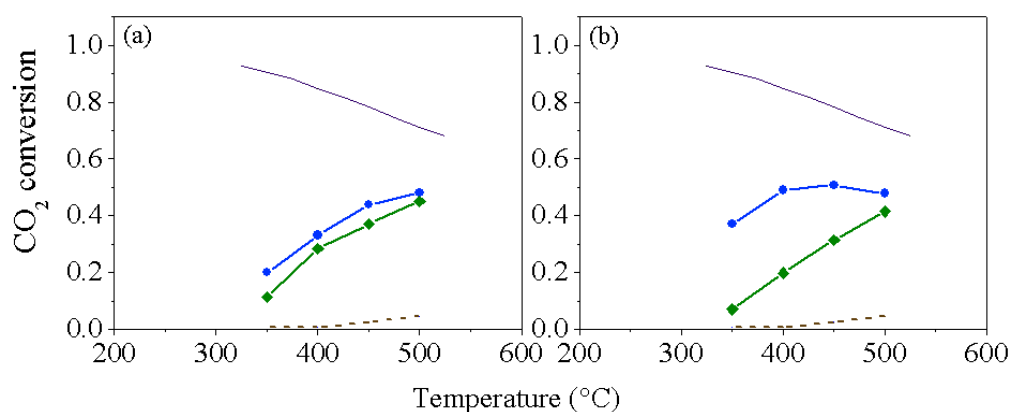
Note that a very small band in the range of 175–350 °C, assigned to reducible NiO species, could only be observed for the Ni-ZrO<sub>2</sub>-SG catalyst. With respect to the high temperature reduction peaks, the Ni-ZrO<sub>2</sub>-cop catalyst showed a maximum at 415 and 550 °C, whereas in the Ni-ZrO<sub>2</sub>-SG catalyst, it was at 440 and 526 °C. It should be mentioned that the highest global hydrogen consumption was obtained with the Ni-ZrO<sub>2</sub>-SG catalyst; therefore, it is inferred that the SMSI was more significant with the Ni-ZrO<sub>2</sub>-cop. In fact, our hydrogen chemisorption results confirmed the findings obtained by TPR, due to the metallic Ni dispersion with both catalysts being <1%, which means that most of the deposited Ni was strongly linked to ZrO<sub>2</sub> [40].

The effect of metal loading on CO<sub>2</sub> conversion with the coprecipitated and sol-gel ZrO<sub>2</sub> support is presented in Figure 5. It can be seen that a higher CO<sub>2</sub> conversion is reached with the 20 wt % Ni/ZrO<sub>2</sub>-COP between 350–450 °C, while, both 10 wt % Ni catalysts presented a similar catalytic performance in the whole temperature range studied. It is worth mentioning that the 20% Ni/ZrO<sub>2</sub>-COP catalyst had the larger surface area in what allowed a better dispersion of nickel particles. In addition, the greater amount of the t-ZrO<sub>2</sub> was also found with the coprecipitated support, which agrees with previous reports [31].

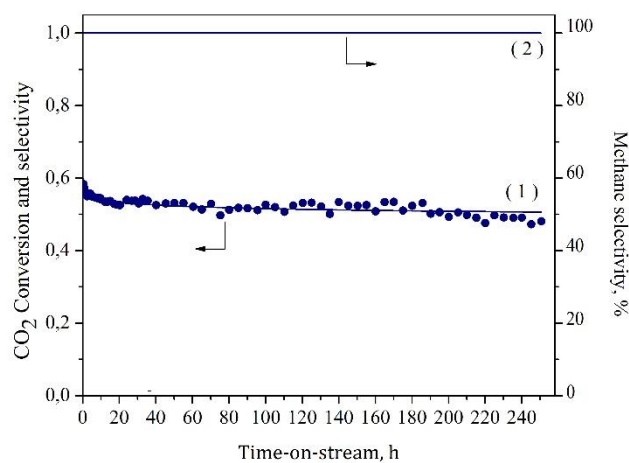
A long-term reaction test was performed for the 20% Ni/ZrO<sub>2</sub>-COP catalyst, as shown in Figure 6. A 58% conversion of CO<sub>2</sub> was observed at the beginning of the reaction test; however, a 10% decay in CO<sub>2</sub> conversion was evidenced during the first 10 h. After this period, CO<sub>2</sub> conversions became stable at 50% on average, up to the 250 h of the experimental test. Methane selectivity remained constant along the test at 100% on a dry basis. The catalyst showed a high thermal stability and a high resistance to deactivation at 400 °C. It is worth noting that previous to the deactivation tests (Figure 5), the effect of GHSV on the CO<sub>2</sub> hydrogenation reaction was evaluated (Figure S3). It was found that after a space velocity of 43,500 mL/ (h gcat) the CO<sub>2</sub> conversion remained constant at about 56%.

Figure 7 shows the Transmission Electron Microscopy (TEM) and High-Resolution Transmission Electron Microscopy (HRTEM) images for 20% Ni/ZrO<sub>2</sub>-COP-F catalyst. The zirconia support was identified by the spacing of  $d = 0.285$  nm and  $0.363$  nm, indexed as (111) and (110), respectively.

The spacing between the two crystal layers of  $d = 0.295$  nm was consistent with the reflection (110), which corresponded to the NiO species.



**Figure 5.** Effect of the preparation method of zirconia supports on CO<sub>2</sub> conversion: (a) 10% Ni content, (b) 20% Ni content. (●) ZrO<sub>2</sub>-COP, (◆) ZrO<sub>2</sub>-SG, (dashed line) SiC, (solid line) equilibrium conversion.



**Figure 6.** Long-term stability test for the 20% Ni/ZrO<sub>2</sub>-COP catalyst. (1) 20% Ni/ZrO<sub>2</sub>-COP. (2) Methane selectivity. Reaction conditions: 400 °C, 0.1 MPa, catalyst 0.1 g, GHSV: 43,500 mL/(h g<sub>Cat</sub>).

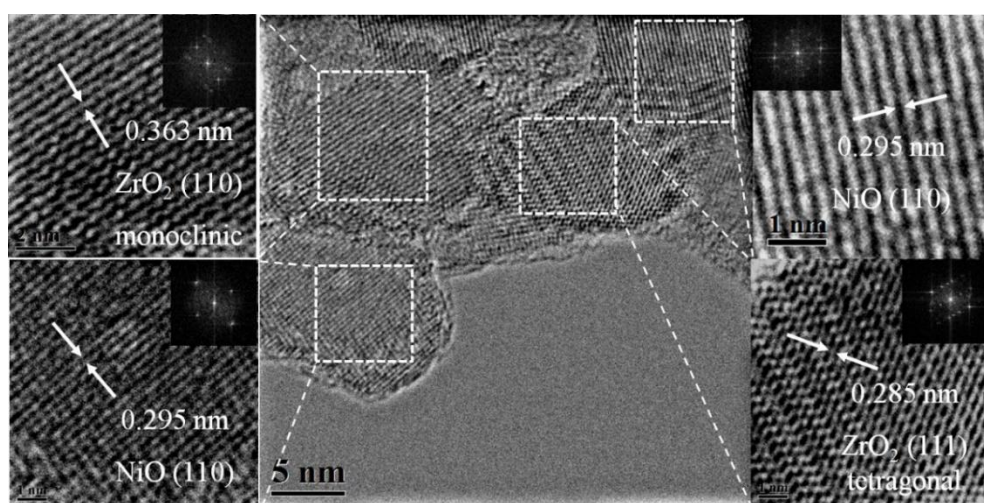


**Figure 7.** Transmission Electron Microscopy (TEM) and High-Resolution Transmission Electron Microscopy (HRTEM) images of 20% NiO/ZrO<sub>2</sub>-COP-F catalyst. The white arrows correspond to the reflections. The inset shows the diffraction pattern showing these reflections.

Figure 8 shows the TEM and HRTEM images for the 20% Ni/ZrO<sub>2</sub>-COP-S catalyst. The zirconia support was identified by the spacing of  $d = 0.281$  nm and  $0.316$  nm, indexed as (111) and (−111), respectively. The spacing between the two crystal layers of  $d = 0.295$  nm was consistent with the reflection (110), which corresponded to a NiO species.

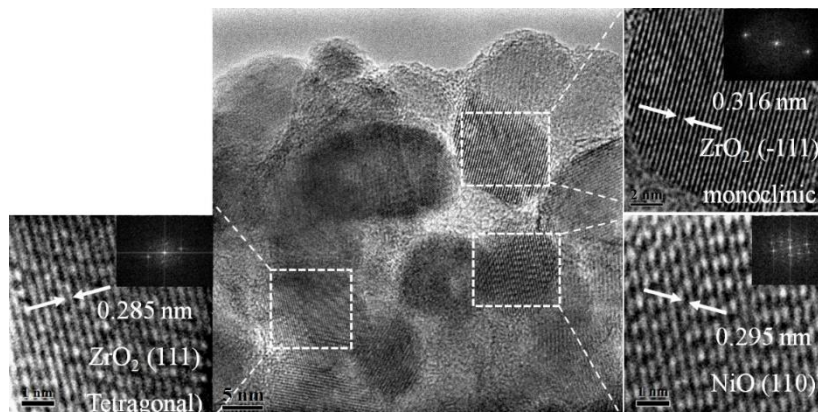


**Figure 8.** TEM and HRTEM images of a 20% Ni/ZrO<sub>2</sub>-COP-S catalyst. The white arrows correspond to the reflections. The inset shows the diffraction pattern showing these reflections.

Hydrogen chemisorption analysis was performed on both the fresh and spent catalysts. Cubic crystal structures [41], and an adsorption stoichiometry factor of two hydrogen atoms per nickel surface atom [42] were considered for calculations. A nickel dispersion of 0.69%, a nickel surface area of  $0.92$  m<sup>2</sup>/g<sub>Cat</sub>, and a mean diameter of nickel particles of 29 nm were obtained for the fresh catalyst, while a nickel dispersion of 0.39%, a nickel surface area of  $0.52$  m<sup>2</sup>/g<sub>Cat</sub>, and a mean diameter of nickel particles of 52 nm were estimated for the spent catalyst. Such differences are mainly related to a slight sintering of nickel particles, which contributes to the loss of catalyst activity during the first hours of the long-term stability test.

The results of X-ray diffraction, Raman spectroscopy, and XPS analysis for the 20% Ni/ZrO<sub>2</sub>-COP-F and 20% Ni/ZrO<sub>2</sub>-COP-S catalysts are presented in Figure 9. Essential differences were observed for the ZrO<sub>2</sub> structure (Figure 9a), mainly in the peaks corresponding to the monoclinic phase at  $2\theta = 24, 28.2, 31.5$  and  $34.2^\circ$ , indicating that in the spent catalyst, the tetragonal phase was predominant. The characteristic Raman peaks (Figure 9b) for the monoclinic phase zirconia were evidenced at 143, 174, 325, 377, and 468, while the characteristic peaks of the tetragonal phase zirconia were observed at 263 and  $632$  cm<sup>−1</sup>. The existence of nickel oxide was confirmed by a signal at  $1099$  cm<sup>−1</sup> in the 20% Ni/ZrO<sub>2</sub>-COP-F catalyst [43–49]. Significant changes in zirconia structure were observed for 20% Ni/ZrO<sub>2</sub>-COP-S catalyst, mainly in the bands exhibited for the monoclinic phase at 175, 325, and  $468$  cm<sup>−1</sup> and those corresponding to nickel oxide at  $776$  and  $956$  cm<sup>−1</sup>, which could be assigned to an Ni–O–Zr interaction. These results can also explain the low metallic dispersion that was observed in fresh and spent catalysts.

Figure 9c–f presents the Zr3d and Ni2p<sub>3/2</sub> XPS spectra of both the fresh and spent nickel zirconia catalysts. As seen in Figure 9c, the fresh catalyst (before activation) was composed of NiO (peaks at 853.4 and 855.3 eV) and a lower amount of Ni(OH)<sub>2</sub>, as indicated by the peaks at 854.9, and 855.7 eV [50]. The presence of these nickel species can be explained by the preparation method. All of the catalyst were calcined in the presence of atmospheric air, and humidity could lead to the formation of Ni(OH)<sub>2</sub>. After the catalyst's activation and evaluation (Figure 9d), NiO and Ni(OH)<sub>2</sub> were also detected; additionally, it was observed the presence of metallic nickel, indicated by the peak at 852 eV [50]. Metallic nickel was formed during the in situ reduction; however, this nickel species is extremely instable, and it can be easily oxidized when it is exposed to air, generating NiO and Ni(OH)<sub>2</sub>. Figure 9e presents the Zr 3d spectrum of the fresh catalyst and Figure 9e presents the spectrum of the spent one.

The spectra of both samples did not show significant changes, and the signals corresponding to the Zr 3d<sub>5/2</sub> transition (181.5 eV) and the Zr 3d<sub>3/2</sub> transition (183.9 eV) were observed.

The Rietveld method was used to quantify the zirconia phase composition of the 20% Ni/ZrO<sub>2</sub>-COP-F and the 20% Ni/ZrO<sub>2</sub>-COP-S catalysts. The results are given in Table 3. When compared with the ZrO<sub>2</sub>-COP support, a slight increase in the monoclinic zirconia phase was observed for the fresh catalyst because of the nickel impregnation, and calcination at 500 °C. The fresh catalyst presents a 1:1 monoclinic to tetragonal ratio; nevertheless, at the end of the stability test, the tetragonal zirconia was the predominant phase. This result was in agreement with the X-ray diffraction, and from Raman spectroscopy, and X-ray photoelectron spectroscopy, significant changes in the monoclinic phase were observed.

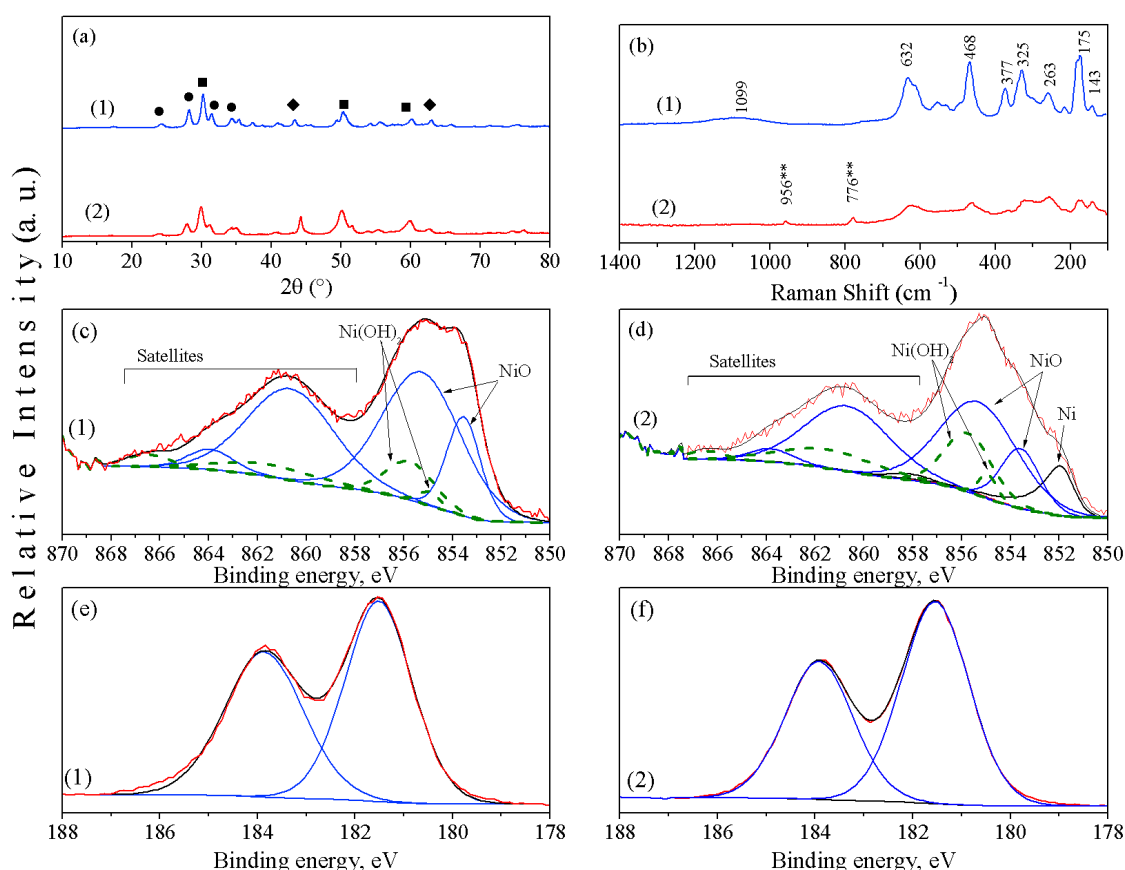


**Figure 9.** Comparative analysis of the fresh and the spent 20% Ni/ZrO<sub>2</sub>-COP catalyst. (a) X-ray diffraction, (b) Raman spectroscopy, (c)–(f) X-ray photoelectron spectroscopy. (1) Spent catalyst, (2) fresh catalyst. ZrO<sub>2</sub> monoclinic phase (●), ZrO<sub>2</sub> tetragonal phase (■), nickel oxide (◆), nickel–zirconia interaction (\*\*).

**Table 3.** Phase composition of the 20% Ni/ZrO<sub>2</sub> catalyst.

Material	Crystalline Phases Composition, %		Monoclinic/Tetragonal Ratio
	Monoclinic	Tetragonal	
ZrO <sub>2</sub> -COP (Support)	47	53	0.88
20% Ni/ZrO <sub>2</sub> -COP-S	40	60	0.66

Since the transition of monoclinic to tetragonal zirconia phase occurs at temperatures that are higher than 1400K [51,52], it was suggested that the changes observed in the monoclinic phase were

mainly related to its degradation. Such degradations could result in oxygen vacancies in the monoclinic phase, which can then act as active sites for the carbon dioxide reduction to methane.

### 3. Experimental

#### 3.1. Support Synthesis

Silicon dioxide (Cabot Corp., Boston, MA, USA) was used as a commercial support ( $\text{SiO}_2$ ). Co-precipitation and the sol-gel route were followed for the synthesis of the zirconia supports. For the co-precipitated zirconia ( $\text{ZrO}_2\text{-COP}$ ), 10 mL of zirconium (IV) butoxide (80 wt % in 1-butanol, Sigma-Aldrich, St. Louis, MO, USA) were dissolved into 150 mL of tert-butyl alcohol (99%, Meyer Corp., Vallejo, CA, USA) under continuous stirring. A concentrated  $\text{NH}_4\text{OH}$  (30%, J.T. Baker, Allentown, PA, USA) solution was added to the mixture until a pH of 9 was obtained. The temperature was raised to 70 °C, and the solution was refluxed for 10 minutes. Afterwards, 26 mL of distilled water was added dropwise to the solution [33]. An immediate formation of a white precipitate was observed. Two different solutions were mixed for the sol-gel zirconium dioxide ( $\text{ZrO}_2\text{-SG}$ ) to be obtained. Solution A was a mixture of 41.25 g zirconium (IV) butoxide, 90 mL of absolute ethyl alcohol (99.9%, Fermont, Monterrey, NL, MEX), and 0.6 mL of nitric acid (70%, Meyer Corp., St. Louis, MO, USA). Solution B was a blend of 6.2 mL of distilled water diluted in 36 mL of absolute ethyl alcohol. Under a nitrogen atmosphere, solution B was added dropwise to solution A under continuous stirring [53]. The resulting white-opaque gel was aged for 24 h. Both  $\text{ZrO}_2\text{-COP}$  and  $\text{ZrO}_2\text{-SG}$  supports were rinsed twice with absolute ethyl alcohol, and dried at 60 °C under air for 12 hours. Dried samples were crushed and calcinated for 2 h in a tube furnace Thermolyne 21,100 at 500 °C at 10 °C/min, and an air flow of 180 mL/min.

Magnesium aluminate spinel was synthesized by a co-precipitation method. Aqueous solutions of 1 M Al and 0.05 M Mg were prepared by using  $\text{Mg}(\text{NO}_3)_2 \cdot 6\text{H}_2\text{O}$  (98%, Caledon, Georgetown, ON, Canada) and  $\text{Al}(\text{NO}_3)_3 \cdot 9\text{H}_2\text{O}$  (98%, Meyer Corp., St. Louis, MO, USA). After that, 200 mL of each solution was mixed under stirring, and then 600 mL of a 0.2 M ammonium carbonate (Sigma-Aldrich, St. Louis, MO, USA) solution with a pH adjusted to 9 was added dropwise [54,55]. The mixture was kept under stirring for 24 h at 50 °C. The precipitate was rinsed twice with absolute ethyl alcohol, and dried at 60 °C under air for 24 h. The dried sample was crushed and calcinated for 2 h in a tube furnace at 900 °C, at 10 °C/min, and with an air flow of 180 mL/min.

#### 3.2. Catalyst Synthesis

$\text{Ni}(\text{NO}_3)_2 \cdot 6\text{H}_2\text{O}$  (J.T. Baker., Allentown, PA, USA) was used as the nickel precursor. Catalysts were prepared by impregnation by using a Hei-Vap rotary evaporator (Heidolph Instruments, Schwabach, Germany) at 55 °C, 60 rpm, and a vacuum pressure of 450 mm Hg. Theoretical nickel contents of 5, 10, 15, and 20 wt % were impregnated on  $\text{SiO}_2$ , and  $\text{MgAl}_2\text{O}_4$  supports, and 10 and 20 wt % were deposited onto  $\text{ZrO}_2$  supports. The resulting materials were crushed, dried at 60 °C for 12 h, and calcined at 500 °C for 4 h in a tubular furnace, with a heating ramp of 10 °C/min, and an air flow of 180 mL/min.

#### 3.3. Catalyst Characterization

X-ray diffraction patterns were recorded on a Siemens D-5000 diffractometer with a copper anode and  $\text{Cu K}\alpha$  radiation over a  $2\theta$  range of 10–80° using a step size of 4°/min. The specific surface area was determined by Nitrogen Physisorption measurements at 77 K, using a Quantachrome Nova e4000 BET Surface Area Analyzer (Quantachrome Instruments, Boynton Beach, FL, USA), outgassing samples at 120 °C for two hours before  $\text{N}_2$  adsorption.

$\text{H}_2$ -pulse chemisorption analysis was performed with 20% Ni/ $\text{ZrO}_2$  catalysts. The measurement was conducted in a ChemBet Pulsar TPR/TPD (Quantachrome Instruments, Boynton Beach, FL, USA) unit equipped with a TCD detector. A catalysts sample of 50 mg was loaded into a U-quartz microreactor, pretreated in nitrogen at 20 mL/min and 90 °C for 1 h, and cooled down to 25 °C in

the same atmosphere. TPR measurements were carried out in a mixture of 5% H<sub>2</sub> balance nitrogen at 25 mL/min, using a heating rate of 10 K/min of up to 650 °C. After TPR analysis, the catalyst was flushed for 30 min under a nitrogen atmosphere at 650 °C, and then cooled down to 25 °C. A gas mixture of 5% H<sub>2</sub> balance nitrogen was pulsed over the catalyst for chemisorption measurements, by using a loop of a known volume of 80 µL for the sequential injections.

A JSM-7800F Field Emission Scanning Electron Microscope (JEOL, Tokyo, Japan) was used for semiquantitative microanalysis, while a JEM-2100F Transmission Electron Microscope (JEOL, Tokyo, Japan) was used for morphology studies. Another characterization of the morphology and microstructure was performed from conventional TEM using an ARM 200CF microscope (JEOL, Tokyo, Japan). For TEM and HRTEM studies, the sample was suspended in ethanol to disperse the powders, and a drop of the sample was deposited on a lacey carbon copper grid as a TEM support. TEM digital images were obtained using a CCD camera and Digital Micrograph software (GMS 3, GATAN, Pleasanton, CA., USA, 2018).

Raman spectroscopy was performed with a Renishaw System 1000 spectrometer (Renishaw, Wotton-under-Edge, Glos, UK) equipped with a green laser (Spectra-Physics (Santa Clara, CA, USA),  $\lambda = 514$  nm, power 19 mW, 1 mW on the sample), under ambient conditions. X-ray photoelectron spectroscopy (XPS) spectra were recorded on a THERMO Scientific K-Alpha spectrometer (Thermo Fisher Scientific, Waltham, MA, USA) equipped with a monochromatic Al<sub>K</sub> X-ray source (1487 eV) and a base pressure of  $1 \times 10^{-9}$  Torr in the analytical chamber. Experimental peaks were decomposed into components using mixed Gaussian–Lorentzian functions and a non-linear squares fitting algorithm. Shirley background subtraction was applied. Binding energies were reproducible to within  $\pm 0.2$  eV, and the C1s peak at 284.6 eV, corresponding to adventitious carbon, was used as a reference.

### 3.4. Catalytic Evaluation

Experimental runs were performed in a “U” shape tubular reactor at atmospheric pressure. Catalysts were reduced in situ before reaction at 450 °C for 1 h, using a 27% (*v/v*) H<sub>2</sub>/Ar stream with a total gas flow of 75 mL/min. Carbon dioxide hydrogenation was conducted at temperatures in the range of 350–500 °C. Hydrogen and carbon dioxide were mixed at a stoichiometric ratio (4:1), the mixture was diluted in argon (50% *v/v*), and the total flow rate was set to 210 mL/min. A total of 0.1 g of catalyst was diluted with 2.5 g of silicon carbide, corresponding to a space velocity of 126,000 mL/(h g<sub>Cat</sub>). The exhaust of the reactor was directed to a gas chromatograph for online analysis. The effect of gas hourly space velocity was studied by using the 20% Ni/ZrO<sub>2-COP</sub> catalyst at 400 °C. The mass of catalyst was varied from 0.1 to 0.5 g, at the flow conditions described earlier. The stability test for this catalyst was carried out at 400 °C at a space velocity of 43,500 mL/(h g<sub>Cat</sub>), using a total flow of 110 mL/min.

## 4. Conclusions

The effects of nickel content on ZrO<sub>2</sub>, SiO<sub>2</sub>, and MgAl<sub>2</sub>O<sub>4</sub>, as well as the effect of the preparation method of zirconia supports, was studied in this work. Nominal metal loads of 5, 10, 15, and 20% of nickel content were used on SiO<sub>2</sub>, and MgAl<sub>2</sub>O<sub>4</sub> supports, while zirconia-based catalysts were impregnated with 10 and 20 wt % metal content. Experimental runs were performed at atmospheric pressure, and at temperatures ranging from 350 to 500 °C, at a constant stoichiometric ratio of H<sub>2</sub>/CO<sub>2</sub> in the feed. An increase in carbon dioxide conversion with an increase in reaction temperature was observed for all catalysts. At 500 °C, Ni/ZrO<sub>2-COM</sub> showed a decrease in CO<sub>2</sub> conversion, which is mainly attributed to the sintering of nickel particles that occur at high temperatures. The 20% Ni/ZrO<sub>2-COP</sub> catalyst resulted in the best performance, with about 50% CO<sub>2</sub> conversion and 100% methane selectivity on a dry basis at 400 °C. On the contrary, the sol-gel zirconia-based catalyst gave the lowest conversions, related to the low specific surface area that was obtained for these materials.

A space velocity of 43,500 mL/(h g<sub>cat</sub>) was found as the optimal value for the evaluation of catalyst stability. The 20% Ni/ZrO<sub>2-COP</sub> catalyst showed high thermal stability, and high resistance to

deactivation at 400 °C for up to 250 h in the experimental run. According to the results, the enhanced catalytic activity and the long-term stability observed with the 20% Ni/ZrO<sub>2</sub>-COP catalyst can be explained regarding the presence of tetragonal zirconia as the significant phase, where Ni nanoparticles were in strong interaction. It is suggested that the formation of oxygen vacancies in the monoclinic phase cause its degradation, and at the same time, they act as active sites for the carbon dioxide reduction to methane.

**Supplementary Materials:** The following are available online at <http://www.mdpi.com/2073-4344/9/1/24/s1>. Table S1. Nickel catalysts reported for CO<sub>2</sub> hydrogenation at atmospheric pressure. Table S2. SEM microanalysis. Table S3. Peak areas of the hydrogen chemisorption analysis. Figure S1. Rietveld simulation for the sol-gel ZrO<sub>2</sub> support. Figure S2. Rietveld simulation for the co-precipitation ZrO<sub>2</sub> support. Figure S3. Effect on GHSV on CO<sub>2</sub> conversion with the 20% Ni/ZrO<sub>2</sub>-COP catalyst. Reaction conditions: 400 °C, 0.1 MPa. Figure S4. SEM images of 20% Ni/ZrO<sub>2</sub>-COP catalysts.

**Author Contributions:** Conceptualization, J.M. and M.A.V.; Methodology, J.M. and M.A.V.; Software, E.H., G.V.A., and E.A.; Validation, J.M., M.A.V., and S.A.; Formal Analysis, J.M., S.A., R.L.M.; Investigation, J.M., E.H., and M.A.V.; Resources, M.A.V., G.V.A., R.L.M.; Data Curation, J.M., M.A.V., S.A.; Writing-Original Draft Preparation, J.M. and M.A.V.; Writing-Review & Editing, J.M., M.A.V., and E.A.; Visualization, E.A.; Supervision, M.A.V.; Project Administration, M.A.V.; Funding Acquisition, M.A.V.

**Funding:** This research received no external funding.

**Acknowledgments:** Authors thank Instituto Politécnico Nacional for financial support of the research project (SIP project 20180063). JMS also thanks to Conacyt for his Postdoctoral Fellowship.

**Conflicts of Interest:** The authors declare no conflict of interest.

## References

1. National Aeronautics and Space Administration (NASA) USA, ClimateChange: Vital Signs of the Planet: Carbon Dioxide. 2017. Available online: <http://climate.nasa.gov/vital-signs/carbon-dioxide/> (accessed on 9 June 2018).
2. Su, X.; Xu, J.; Liang, B.; Duan, H.; Hou, B.; Huang, Y.J. Catalytic carbon dioxide hydrogenation to methane: A review of recent studies. *J. Energy Chem.* **2016**, *25*, 553–565. [[CrossRef](#)]
3. Ronsch, S.; Schneider, J.; Matthischke, S.; Schluter, M.; Gotz, M.; Lefebvre, J.; Prabhakaran, P.; Bajohr, S. Review on methanation—From fundamentals to current projects. *Fuel* **2016**, *166*, 276–296. [[CrossRef](#)]
4. Aziz, M.A.A.; Jalil, A.A.; Triwahyono, S.; Ahmad, A. CO<sub>2</sub> methanation over heterogeneous catalysts: Recent progress and future prospects. *Green Chem.* **2015**, *17*, 2647–2663. [[CrossRef](#)]
5. Wang, W.; Gong, J. Methanation of carbon dioxide: An overview. *Front. Chem. Sci. Eng.* **2011**, *5*, 2–10. [[CrossRef](#)]
6. Younas, M.; Kong, L.; Bashir, M.J.K.; Nadeem, H.; Shehzad, A.; Sethupathi, S. Recent Advancements, Fundamental Challenges, and Opportunities in Catalytic Methanation of CO<sub>2</sub>. *Energy Fuels* **2016**, *30*, 8815–8831. [[CrossRef](#)]
7. Li, W.; Wang, H.; Jiang, X.; Zhu, J.; Liu, Z.; Guo, X.; Song, C. A short review of recent advances in CO<sub>2</sub> hydrogenation to hydrocarbons over heterogeneous catalysts. *RSC Adv.* **2018**, *8*, 7651–7669. [[CrossRef](#)]
8. Frontera, P.; Macario, A.; Ferraro, M.; Antonucci, P.L. Supported Catalysts for CO<sub>2</sub> Methanation: A Review. *Catalysts* **2017**, *7*, 59. [[CrossRef](#)]
9. Ghaib, K.; Ben-Fares, F.Z. Power-to-Methane: A state-of-the-art review. *Renew. Sustain. Energy Rev.* **2018**, *81*, 433–446. [[CrossRef](#)]
10. Gao, J.; Liu, Q.; Gu, F.; Liu, B.; Zhong, Z.; Su, F. Recent advances in methanation catalysts for the production of synthetic natural gas. *RSC Adv.* **2015**, *5*, 22759–22776. [[CrossRef](#)]
11. Ren, J.; Qin, X.; Yang, J.Z.; Qin, Z.F.; Guo, H.L.; Lin, J.Y.; Li, Z. Methanation of carbon dioxide over Ni-M/ZrO<sub>2</sub> (M = Fe, Co, Cu) catalysts: Effect of addition of a second meta. *Fuel Process. Technol.* **2015**, *137*, 204–211. [[CrossRef](#)]
12. Ando, H.; Pujiwara, M.; Matsumura, Y.; Miyamura, H.; Souma, Y. Methanation of carbon dioxide over LaNi<sub>4</sub>X type catalysts. *Energy Convers. Manag.* **1995**, *36*, 653–656. [[CrossRef](#)]
13. Abelló, S.; Berruero, C.; Montané, D. High-loaded nickel–alumina catalyst for direct CO<sub>2</sub> hydrogenation into synthetic natural gas (SNG). *Fuel*. **2013**, *113*, 598–609. [[CrossRef](#)]

14. Song, H.; Yang, J.; Zhao, J.; Chou, L. Methanation of Carbon Dioxide over a Highly Dispersed Ni/La<sub>2</sub>O<sub>3</sub> Catalyst. *Chin. J. Catal.* **2010**, *31*, 21–23. [[CrossRef](#)]
15. Ussa, P.A.; Ocampo, F.; Kobl, K.; Louis, B.; Thibault-Starzyka, F.; Daturi, M.; Bazin, P.; Thomas, S.; Roger, A.C. Catalytic CO<sub>2</sub> valorization into CH<sub>4</sub> on Ni-based ceria-zirconia. Reaction mechanism by operando IR spectroscopy. *Catal. Today* **2013**, *215*, 201–207. [[CrossRef](#)]
16. Graca, I.; González, L.V.; Bacariza, M.C.; Fernandes, A.; Henriques, C.; Lopes, J.M.; Ribeiro, M.F. CO<sub>2</sub> hydrogenation into CH<sub>4</sub> on NiHNaUSY zeolites. *Appl. Catal. B Environ.* **2014**, *147*, 101–110. [[CrossRef](#)]
17. Xu, J.; Lin, Q.; Su, X.; Duan, H.; Geng, H.; Huang, Y. CO<sub>2</sub> methanation over TiO<sub>2</sub>–Al<sub>2</sub>O<sub>3</sub> binary oxides supported Ru catalysts. *Chin. J. Chem. Eng.* **2016**, *24*, 140–145. [[CrossRef](#)]
18. Ocampo, F.; Louis, B.; Kiwi-Minsker, L. Effect of Ce/Zr composition and noble metal promotion on nickel based Ce<sub>x</sub>Zr<sub>1-x</sub>O<sub>2</sub> catalysts for carbon dioxide methanation. *Appl. Catal. A Gen.* **2011**, *392*, 36–44. [[CrossRef](#)]
19. Liu, H.; Zou, X.; Wang, X.; Lu, X.; Ding, W. Effect of CeO<sub>2</sub> addition on Ni/Al<sub>2</sub>O<sub>3</sub> catalysts for methanation of carbon dioxide with hydrogen. *J. Nat. Gas Chem.* **2012**, *21*, 703–707. [[CrossRef](#)]
20. Zhi, G.; Guo, X.; Wang, Y.; Jin, G.; Guo, X. Effect of La<sub>2</sub>O<sub>3</sub> modification on the catalytic performance of Ni/SiC for methanation of carbon dioxide. *Catal. Commun.* **2011**, *16*, 56–59. [[CrossRef](#)]
21. Zhen, W.; Li, B.; Lu, G.; Ma, J. Enhancing catalytic activity and stability for CO<sub>2</sub> methanation on Ni@MOF-5 via control of active species dispersion. *Chem. Commun.* **2015**, *51*, 1728–1731. [[CrossRef](#)]
22. Ocampo, F.; Louis, B.; Roger, A.C. Methanation of carbon dioxide over nickel-based Ce<sub>0.72</sub>Zr<sub>0.28</sub>O<sub>2</sub> mixed oxide catalysts prepared by sol–gel method. *Appl. Catal. A Gen.* **2009**, *369*, 90–96. [[CrossRef](#)]
23. Gao, J.; Jia, L.S.; Fang, W.P.; Li, Q.B.; Song, H. Methanation of carbon dioxide over the LaNiO<sub>3</sub> perovskite catalysts activated under the reactant stream. *J. Fuel Chem. Technol.* **2009**, *37*, 573–577. [[CrossRef](#)]
24. Mutz, B.; Carvalho, H.W.P.; Mangold, S.; Kleist, W.; Grunwaldt, J.D. Methanation of CO<sub>2</sub>: Structural response of a Ni-based catalyst under fluctuating reaction conditions unraveled by operando spectroscopy. *J. Catal.* **2015**, *327*, 48–53. [[CrossRef](#)]
25. Tada, S.; Shimizu, T.; Kameyama, H.; Haneda, T.; Kikuchi, R. Ni/CeO<sub>2</sub> catalysts with high CO<sub>2</sub> methanation activity and high CH<sub>4</sub> selectivity at low temperatures. *Int. J. Hydrogen Energy* **2012**, *37*, 5527–5531. [[CrossRef](#)]
26. Frey, M.; Édouard, D.; Roger, A.C. Optimization of structured cellular foam-based catalysts for low-temperature carbon dioxide methanation in a platelet milli-reactor. *CR Chim.* **2015**, *18*, 283–292. [[CrossRef](#)]
27. Tada, S.; Ochieng, O.J.; Kikuchi, R.; Haneda, T.; Kameyama, H. Promotion of CO<sub>2</sub> methanation activity and CH<sub>4</sub> selectivity at low temperatures over Ru/CeO<sub>2</sub>/Al<sub>2</sub>O<sub>3</sub> catalysts. *Int. J. Hydrogen Energy* **2014**, *39*, 10090–10100. [[CrossRef](#)]
28. Bakar, W.A.W.A.; Ali, R.; Mohammad, N.S. The effect of noble metals on catalytic methanation reaction over supported Mn/Ni oxide based catalysts. *Arab. J. Chem.* **2015**, *8*, 632–643. [[CrossRef](#)]
29. Chen, K.; Xie, S.; Iglesia, E.; Bell, A.T. Structure and Properties of Zirconia-Supported Molybdenum Oxide Catalysts for Oxidative Dehydrogenation of Propane. *J. Catal.* **2000**, *189*, 421–430. [[CrossRef](#)]
30. Chary, J.K.V.R.; Ramesh, K.; Naresh, D.; Rao, P.V.R.; Rao, V.V. The effect of zirconia polymorphs on the structure and catalytic properties of V<sub>2</sub>O<sub>5</sub>/ZrO<sub>2</sub> catalysts. *Catal. Today* **2009**, *141*, 187–194. [[CrossRef](#)]
31. Yamasaki, M.; Habazaki, H.; Asami, K.; Izumiya, K.; Hashimoto, K. Effect of tetragonal ZrO<sub>2</sub> on the catalytic activity of Ni/ZrO<sub>2</sub> catalyst prepared from amorphous Ni–Zr alloys. *Catal. Commun.* **2006**, *7*, 24–28. [[CrossRef](#)]
32. Solis-Garcia, A.; Louvier-Hernandez, J.F.; Almendarez-Camarillo, A.; Fierro-Gonzalez, J.C. Participation of surface bicarbonate, formate and methoxy species in the carbon dioxide methanation catalyzed by ZrO<sub>2</sub>-supported Ni. *Appl. Catal. B* **2017**, *218*, 611–620. [[CrossRef](#)]
33. Bokhimj, X.; Morales, A.; Novaro, O.; Portilla, M.; López, T.; Tzompantzi, F.; Gómez, R. Tetragonal Nanophase Stabilization in Nondoped Sol–Gel Zirconia Prepared with Different Hydrolysis Catalysts. *J. Solid State Chem.* **1998**, *135*, 28–35. [[CrossRef](#)]
34. Knoblauch, N.; Simon, H.; Dörrer, L.; Uxa, D.; Beschnitt, S.; Fielitz, P.; Wendelstorf, J.; Spitzer, K.H.; Schmücker, M.; Borchardt, G. Ceria: Recent Results on Dopant-Induced Surface Phenomena. *Inorganics* **2017**, *5*, 76. [[CrossRef](#)]
35. Kaminski, P.; Ziolenka, M.; van Bokhovenbc, J.A. Mesoporous cerium–zirconium oxides modified with gold and copper—synthesis, characterization and performance in selective oxidation of glycerol. *RSC Adv.* **2017**, *7*, 7801–7819. [[CrossRef](#)]

36. Rahman, A.; Jayaganthan, R. Study of photocatalyst magnesium aluminate spinel nanoparticles. *J. Nanostruct. Chem.* **2015**, *5*, 147–151. [[CrossRef](#)]
37. Morris, M.C.; McMurdie, H.F.; Evans, E.H.; Paretzkin, B.; Parker, H.S.; Panagiotopoulos, N.C. Standard X-ray Diffraction Powder Patterns. National Bureau of Standards Monograph, October 1981. Available online: <https://nvlpubs.nist.gov/nistpubs/Legacy/MONO/nbsmonograph25-5.pdf> (accessed on 9 June 2018).
38. Thao, N.T.; Nhu, N.T. Evaluation of catalytic activity of MeOx/sepiolite in benzyl alcohol oxidation. *JS: AMD* **2018**, *3*, 289–295. [[CrossRef](#)]
39. Sehested, J.; Gelten, J.A.P.; Remediakis, I.N.; Bengaard, H.; Nørskov, J.K. Sintering of nickel steam-reforming catalysts: Effects of temperature and steam and hydrogen pressures. *J. Catal.* **2004**, *223*, 432–443. [[CrossRef](#)]
40. Meng, F.; Li, Z.; Ji, F.; Li, M. Effect of ZrO<sub>2</sub> on catalyst structure and catalytic methanation performance over Ni-based catalyst in slurry-bed reactor. *Int. J. Hydrogen Energy* **2015**, 8833–8843. [[CrossRef](#)]
41. Bergeret, G.; Gallezot, P. Particle size and dispersion measurements. *Handb. Heterog. Catal.* **2008**, *1*, 738–765. [[CrossRef](#)]
42. Lowell, S.; Shields, J.E.; Thomas, M.A. *Characterization of Porous Solids and Powders: Surface Area, Pore Size and Density*; Springer: Berlin, Germany, 2006; pp. 212–232. ISBN 978-1-4020-2303-3.
43. Pomfret, M.B.; Owrutsky, J.C.; Walker, R.A. High-Temperature Raman Spectroscopy of Solid Oxide Fuel Cell Materials and Processes. *J. Phys. Chem. B* **2006**, *110*, 17305–17308. [[CrossRef](#)]
44. Mironova-Ulmane, N.; Kuzmin, A.; Steins, I.; Grabis, J.; Sildos, I.; Pärs, M. Raman scattering in nanosized nickel oxide NiO. *J. Phys. Conf. Ser.* **2007**, *93*, 012039. [[CrossRef](#)]
45. Agarkov, D.A.; Burmistrov, I.N.; Tsybrov, F.M.; Tartakovskii, I.I.; Kharton, V.V.; Bredikhin, S.I. In-situ Raman spectroscopy analysis of the interfaces between Ni-based SOFC anodes and stabilized zirconia electrolyte. *Solid State Ion.* **2017**, *302*, 133–137. [[CrossRef](#)]
46. Hall, D.S.; Lockwood, D.J.; Poirier, S.; Bock, C.; MacDougall, B.R. Raman and infrared spectroscopy of  $\alpha$  and  $\beta$  phases of thin nickel hydroxide films electrochemically formed on nickel. *J. Phys. Chem. A* **2012**, *116*, 6771–6784. [[CrossRef](#)] [[PubMed](#)]
47. Zhao, B.; Xu, X.; Gao, J.; Fu, Q.; Tang, Y. Structure Characterization of WO<sub>3</sub>/ZrO<sub>2</sub> Catalysts by Raman Spectroscopy. *J. Raman Spectrosc.* **1996**, *27*, 549–554. [[CrossRef](#)]
48. Baklanova, N.I.; Kolesov, B.A.; Zima, T.M. Raman study of yttria-stabilized zirconia interfacial coatings on Nicalon™ fiber. *J. Eur. Ceram. Soc.* **2007**, *27*, 165–171. [[CrossRef](#)]
49. Li, M.; Feng, Z.; Xiong, G.; Ying, P.; Xin, Q.; Li, C. Phase Transformation in the Surface Region of Zirconia Detected by UV Raman Spectroscopy. *J. Phys. Chem. B* **2001**, *105*, 8107–8111. [[CrossRef](#)]
50. Biesinger, M.C.; Payne, B.P.; Lau, L.W.M.; Gerson, A.; Smart, R.S.C. X-ray photoelectron spectroscopic chemical state quantification of mixed nickel metal, oxide and hydroxide systems. *Surf. Interface Anal.* **2009**, *41*, 324–332. [[CrossRef](#)]
51. Cao, W.; Kang, J.; Fan, G.; Yang, L.; Li, F. Fabrication of Porous ZrO<sub>2</sub> Nanostructures with Controlled Crystalline Phases and Structures via a Facile and Cost-Effective Hydrothermal Approach. *Ind. Eng. Chem. Res.* **2015**, *54*, 12795–12804. [[CrossRef](#)]
52. Xie, S.; Iglesia, E.; Bell, A.T. Water-Assisted Tetragonal-to-Monoclinic Phase Transformation of ZrO<sub>2</sub> at Low Temperatures. *Chem. Mater.* **2000**, *12*, 2442–2447. [[CrossRef](#)]
53. Stocker, C.; Schneider, M.; Baiker, A. Zirconia aerogels and xerogels: Influence of solvent and acid on structural properties. *J. Porous Mater.* **1995**, *2*, 171–183. [[CrossRef](#)]
54. Wajler, A.; Tomaszewski, H.; Weglarz, H.; Diduszko, R. Influence of processing on magnesium aluminate precursors morphology prepared by co-precipitation. *Ceram. Mater.* **2011**, *63*, 104–108.
55. Li, J.G.; Ikegami, T.; Lee, J.H.; Mori, T.; Yajima, Y. Synthesis of Mg–Al spinel powder via precipitation using ammonium bicarbonate as the precipitant. *J. Eur. Ceram. Soc.* **2001**, *21*, 139–148. [[CrossRef](#)]

